Progress Towards On-Road Aerodynamic-State Estimation in Traffic

Brian R. McAuliffe[1], Moira Barnes[2], Taufiq Rahman[1], Abdullah Jirjees[1],
Faegheh Ghorbanishohrat[1], David Rival[2]

[1]National Research Council Canada
1200 Montreal Rd., Ottawa, Ontario, Canada, K1A 0R6

[2]RivalLab/ Queen’s University
99 University Avenue, Kingston, Ontario, Canada, K7L 3N6

Email: Brian.McAuliffe@ nrc-cnrc.gc.ca

Abstract: By exploiting aerodynamic interactions among road vehicles, driving-automation technologies have the potential to reduce energy use and emissions. Traditional platooning concepts consider multiple vehicles travelling in close longitudinal proximity within the same road lane, but recent research suggests that lateral offsetting and adjacent-lane positioning can provide additional benefits in the complex traffic-and-wind climate experienced in everyday driving. On-road aerodynamic-state estimation will be a critical feedback metric for such autonomous-vehicle systems. A small sample of multi-vehicle wind-tunnel results is used to introduce a concept for using surface-pressure differences to infer aerodynamic states, and measurements from on-road in-traffic tests highlight ways to differentiate between wake effects from leading vehicles and close-proximity pressure-field influences from adjacent-lane vehicles. Complex conditions and varied positions of other vehicles in traffic highlight the need to track temporal changes in states, and to use multiple metrics to predict aerodynamic states.

1 Concept and Objectives

Instantaneous aerodynamic load prediction, whether for air or ground vehicles, has vast applications related to performance, energy use, stability, and safety. Transient disturbances from wind gusts, dynamic body motion, or relative motion to proximate objects pose significant challenges. Current advances in autonomous aerial and road mobility are pushing the limits of necessary environmental feedback to ensure reliable control of vehicle motion and to ensure safety, while exploiting or avoiding aerodynamic interactions with other bodies. Examples include: urban air-mobility applications for human and goods transportation, for which navigating buildings and associated wind disturbances is important [1], and autonomous road-traffic systems,

Contribution: 2025 FKFS Conference on Vehicle Aerodynamics and Thermal Management
15 – 16 October 2025 | Leinfelden-Echterdingen

for which close-proximity driving can reduce congestion and save energy via speed harmonization and aerodynamic interactions [2]. Sensing the aerodynamic state of a vehicle directly may improve real-time control strategies. Biological systems use sensory feedback in this manner, such as fish or birds adapting in real time to exploit local aero/hydro-dynamic phenomena [3]. Drones and ground vehicles are bluff bodies (non-streamlined), for which surface-pressure changes, rather than air friction, are highly correlated with overall aerodynamic performance, and can be used to infer local wind conditions and aerodynamic behaviour [4]. Recent work has demonstrated the feasibility of using sparse arrays of surface-pressure measurements to infer the aerodynamic state of a body, by making use of data-driven methods via transition-network concepts [5]. This approach is particularly useful for non-linear aerodynamic environments with separated/stalled flows, characteristic of bluff bodies.

Emerging traffic-aerodynamics research and the accelerating deployment of connected-and-automated-vehicle (CAV) and intelligent-transportation-systems (ITS) technologies suggests that road-vehicle aerodynamic drag, and associated energy use, can be optimized via two approaches: 1) optimized multi-lane mixed-traffic patterns that minimize traffic-system drag [6]; and 2) active aerodynamic technologies that adapt to their traffic environment [7]. This paper describes the preliminary steps of a project examining the first of these approaches, namely traffic-aerodynamic optimization using CAV technologies. Within this project, named *AeroCAV*, an attempt is being made to apply wireless surface-pressure sensing with a transition-network approach to estimate real-time aerodynamic performance. Section 2 provides some context to the necessity of the approaches being applied, while Sections 3 and 4 document the on-road demonstrator and some preliminary measurements, respectively.

2 The Challenge of Characterizing Aerodynamic Boundary Conditions

Based on a previous proof-of-concept investigation using a wireless-surface-pressure measurement system [8], pressure-difference coefficients calculated using a vehicle-speed-based dynamic pressure showed suitability as indicators of aerodynamic boundary conditions. Building upon that experience, with additional knowledge from wind tunnel tests of traffic interactions [6,9], three pressure-coefficient parameters have been selected for the current on-road investigations, based on six locations around the perimeter of the test vehicle. Specific locations are the Front centre (F), the Back/Base centre (B), the Left-side door (L), the Right-side door (R), the Front Left bumper (FL), and the Front Right bumper (FR). The (F)ront position is intended to be as close to the stagnation point as possible. Pressure-difference coefficients are defined based on the front-to-back difference ($\Delta\bar{C}_{\mathrm{p}}^{FB}$), the left-to-right-door difference ($\Delta\bar{C}_{\mathrm{p}}^{LR}$), and the front-bumper left-to-right difference ($\Delta\bar{C}_{\mathrm{p}}^{FLR}$). Challenges, and potential solutions, using these parameters are described to provide some context for the on-road data presented in a later section.

The three pressure-difference metrics have been calculated and presented in this section for four traffic scenarios that were simulated using a 30%-scale DrivAer model in the NRC 9 m Wind Tunnel. Configuration 1 consists of the isolated DrivAer Notchback model in uniform flow. Configurations 2 and 3 consist of the DrivAer in proximity to an AeroSUV model, in a side-by-side arrangement (see Figure 1) and a longitudinal-following arrangement (following the AeroSUV at 2 vehicle-length spacing). Configuration 4 consists of a side-by-side arrangement with a heavy-duty-vehicle (HDV) model, with the base of the two model nearly coincident (see [10] for details of the HDV model).

Figure 1: 30%-scale DrivAer and AeroSUV models in a side-by-side configuration in the NRC 9 m Wind Tunnel.

Figure 2 shows the variation with yaw angle of the $\Delta\bar{C}_{\mathrm{p}}^{FB}$, $\Delta\bar{C}_{\mathrm{p}}^{LR}$, and $\Delta\bar{C}_{\mathrm{p}}^{FLR}$ parameters, using the wind-speed-based $\Delta\bar{C}_{P}$ values from the wind-tunnel measurements. Although base pressure generally decreases with increasing yaw angle, the corresponding lateral shift of the front stagnation point away from the centreline causes a decrease at the front-centre position, which is approximately equal to the change in base pressure. This results in an insensitivity of the $\Delta\bar{C}_{\mathrm{p}}^{FB}$parameter to yaw angle for this DrivAer shape. This behaviour suggests that $\Delta\bar{C}_{\mathrm{p}}^{FB}$ may be a good indicator of dynamic pressure experienced by the vehicle. The lateral pressure differences, at the front of the body ($\Delta\bar{C}_{\mathrm{p}}^{LR}$) or from door to door ($\Delta\bar{C}_{\mathrm{p}}^{FLR}$), show near-linear changes with yaw angle, which suggest that either of these parameters may be a good indicator of the yaw angle experienced by the vehicle. The main difference between $\Delta\bar{C}_{\mathrm{p}}^{FLR}$ and $\Delta\bar{C}_{\mathrm{p}}^{LR}$ is the slope, with the former having five times the sensitivity of the latter.

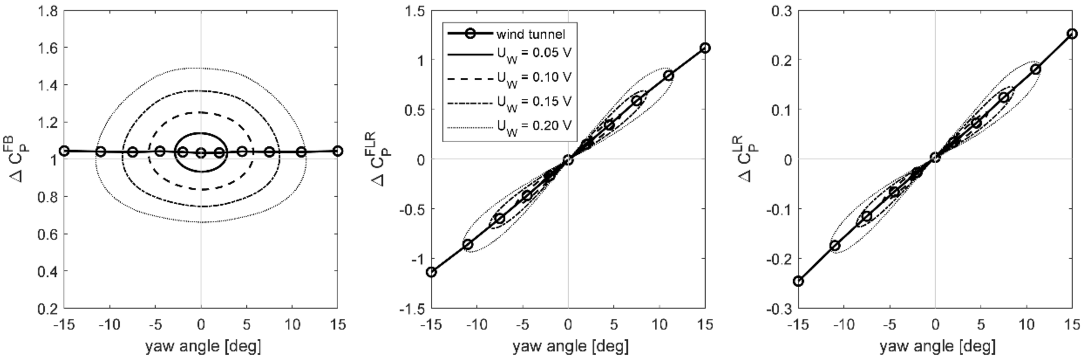

Figure 2: $\Delta\bar{C}_P$ metrics from wind-tunnel tests of the isolated DrivAer model.

Figure 2 estimates the variation of the three $\Delta\bar{C}_P$ parameters that would arise when encountering different terrestrial wind speeds (increments of 5% of vehicle speed, up to 20%). These $\Delta\bar{C}_P$ variations were calculated using a dynamic pressure based on the vehicle speed, not the apparent wind speed. For each of the wind-speed increments, the data show a path representing a 360° change in the direction of the wind relative to the direction of motion of the vehicle. Head- and tail-wind conditions scale the near-zero-yaw-angle values to greater or lesser magnitudes, while cross-wind conditions increase the yaw angle. This is particularly apparent for the front-to-back $\Delta\bar{C}_\mathrm{p}^{FB}$ parameter which shows up to a ±40% change at 0° yaw angle associated with the 20% wind-speed increment, again suggesting that it may be a good indicator of the dynamic-pressure of the wind. In a cross-wind orientation, the 20% wind speed generates yaw angles that reach about 11°. The incremental $\Delta\bar{C}_\mathrm{p}^{LR}$ and $\Delta\bar{C}_\mathrm{p}^{FLR}$ values, when terrestrial wind effects are estimated, show small changes at low wind speeds, and extend reasonably proportionally with yaw angle as cross winds increases. If measured on a vehicle, the $\Delta\bar{C}_P$ characteristics shown in Figure 2 suggest that these parameters can be used to estimate the wind conditions (speed and yaw angle) while driving. Either $\Delta\bar{C}_\mathrm{p}^{LR}$ or $\Delta\bar{C}_\mathrm{p}^{FLR}$ could be used to first estimate the yaw angle, while the estimated yaw angle and the $\Delta\bar{C}_\mathrm{p}^{FB}$ parameter could be used to infer the dynamic pressure, and correspondingly the wind speed. With appropriate characterization, this boundary-condition estimation can be related to performance metrics, like the drag coefficient, to estimate the “aerodynamic state” of the vehicle.

When travelling in traffic, significant challenges can arise that invalidate the relationships of $\Delta\bar{C}_\mathrm{p}^{FB}$, $\Delta\bar{C}_\mathrm{p}^{LR}$, and $\Delta\bar{C}_\mathrm{p}^{FLR}$ as direct indicators of local aerodynamic boundary conditions. Some of these challenges are highlighted in Figure 3 that compares the variability of these $\Delta\bar{C}_P$ parameters in different wind conditions for specific traffic-interaction conditions. The isolated vehicle case is contrasted against the “side by side SUV” case, the “following an SUV” case, and the “side by side HDV” case, based on the wind-tunnel measurements. For each case, the symbol represents the 0°-yaw-angle value that represents no-wind conditions, and the lines represent the same terrestrial-wind magnitudes of Figure 2. There is no general consistency in the magnitudes and trends of the $\Delta\bar{C}_P$ characteristics amongst the various cases. The "side by side SUV" is similar to the "isolated" case for the $\Delta\bar{C}_\mathrm{p}^{FB}$ parameter, but has distinct and opposite offsets for the $\Delta\bar{C}_\mathrm{p}^{LR}$ and $\Delta\bar{C}_\mathrm{p}^{FLR}$ parameters with some reduction in linearity. When "following an SUV", a distinct downward shift is observed for $\Delta\bar{C}_\mathrm{p}^{FB}$, and reductions in slope and linearity are observed for $\Delta\bar{C}_\mathrm{p}^{LR}$ and $\Delta\bar{C}_\mathrm{p}^{FLR}$. The "side by side HDV" case differs in that it demonstrates significant yaw asymmetry in all three parameters, the largest spread of $\Delta\bar{C}_\mathrm{p}^{FB}$ values, and non-monotonic variability with yaw angle.

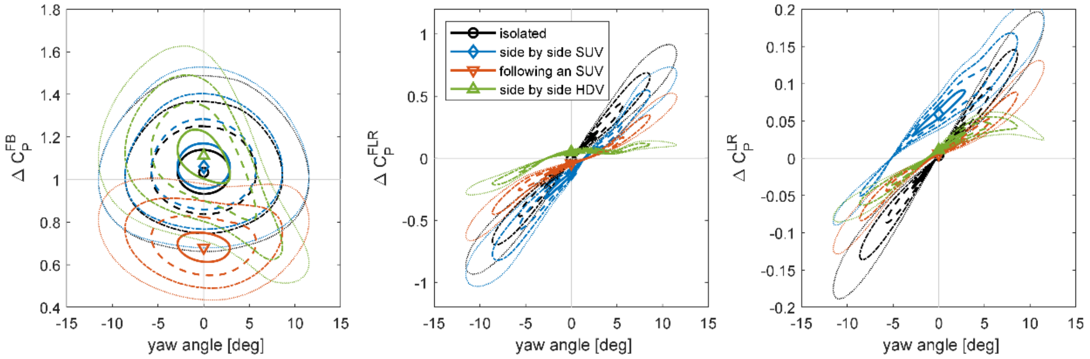

Figure 3: $\Delta\bar{C}_P$ metrics in various on-road scenarios relative to yaw angle.

These varying characteristics in the $\Delta\bar{C}_P$ plots of Figure 3 make prediction of local boundary conditions much more complicated than isolated-vehicle results would suggest. For example, if a yaw angle is inferred from $\Delta\bar{C}_\mathrm{p}^{LR}$ and $\Delta\bar{C}_\mathrm{p}^{FLR}$, the variability of the $\Delta\bar{C}_\mathrm{p}^{FB}$ parameter amongst different conditions will make an accurate estimation of the local wind speed nearly impossible. However, the manner in which the scenarios differ from each other suggests that multi-variable or multi-state approaches may provide a solution to estimate the "aerodynamic state" of the vehicle. Figure 4 shows these types of multi-state relationships for the data of Figure 3, but with the $\Delta\bar{C}_P$ parameters plotted against each other instead of against yaw angle. Significant variation is again seen for the $\Delta\bar{C}_\mathrm{p}^{FB}$ plots (left and middle), while the $\Delta\bar{C}_\mathrm{p}^{LR}$ vs. $\Delta\bar{C}_\mathrm{p}^{FLR}$ plot shows some collapsing of data along distinct characteristics for some of the traffic-interaction scenarios. Combined with transition-network concepts [5], a suitable approach to aerodynamic-state estimation may be feasible. This concept of this project intends to use sparse sensor data captured on the test vehicle and combined with a pre-trained algorithm to provide an estimate of the present aerodynamic state. By embedding these measurements into a reduced-order phase-space model, the system can then characterize distinct aerodynamic regimes and quantify the likelihood of transitions between them. Transition-network concepts, coupled with Bayesian statistics, will provide the framework for eventually estimating the current aerodynamic state in real time. The final result will provide a low-order representation of the inherently non-linear vehicle-flow interactions, which should remain robust to the elevated noise levels typical of experimental on-road pressure measurements. The remainder of this paper describes preliminary results from an on-road demonstrator being developed that will make use of these concepts, amongst other sensor-fusion approaches, to adopt aerodynamic-state estimation as a control metric for minimizing energy use of automated multi-vehicle-traffic systems. Preliminary measurements of the $\Delta\bar{C}_\mathrm{p}^{FB}$, $\Delta\bar{C}_\mathrm{p}^{LR}$, and $\Delta\bar{C}_\mathrm{p}^{FLR}$ metrics are shown to demonstrate the potential feasibility of boundary-condition estimation from on-road measurements.

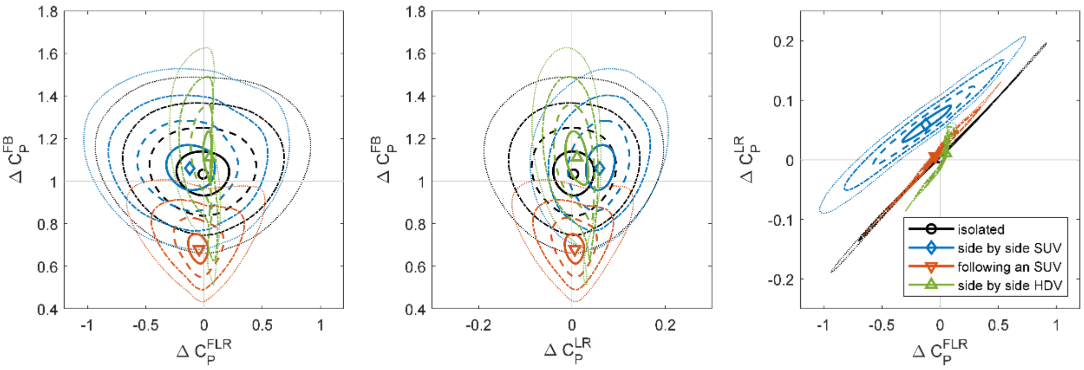

Figure 4: $\Delta\bar{C}_P$ metrics in various on-road scenarios relative to each other.

3 On-Road Tests

An on-road demonstrator is being developed for the AeroCAV project with its end-use goal to provide a platform to demonstrate the potential for energy savings from controlled aerodynamic optimization with respect to wind and traffic conditions. The system will be interchangeable on a number of vehicles. For initial concept evaluation, the first use is with a compact battery-electric SUV. This section documents the vehicle system, the initial test conditions, and the data processing methods.

3.1 Vehicle Systems

The experimental platform consisted of a 2022 Hyundai Ioniq 5 instrumented with a Robotic Operating System (ROS)-based multimodal data acquisition system developed in-house (Figure 5). The platform integrates multiple temporally synchronized perception and vehicle-state sensing nodes. Two RGB cameras were mounted at the front and rear of the vehicle to capture forward- and backward-facing video. An Ouster OS1 LiDAR was installed to provide 3D point cloud data for depth perception and object detection. Vehicle dynamics and reference pressure measurements were recorded using an Xsens MTi-710 Inertial Measurement Unit (IMU) sensor, installed inside the cabin. Eight Bluetooth Low Energy (BLE)-enabled pressure sensors (Arduino Nano 33 BLE Sense Rev2) were mounted around the vehicle—three on the front bumper, one on the roof, one on the driver's side door, one on the passenger's side door, and one on the rear door. An additional sensor was deployed to measure ambient temperature outside the vehicle. All BLE nodes streamed pressure or temperature readings to the ROS ecosystem. Vendor supplied drivers along with custom microcontroller firmware and ROS drivers were developed to interface the BLE-enabled pressure and temperature sensors, enabling time synchronized acquisition and storage of camera images, LiDAR scans, IMU readings, and pressure/temperature values within a unified ROS bag-based data collection framework.

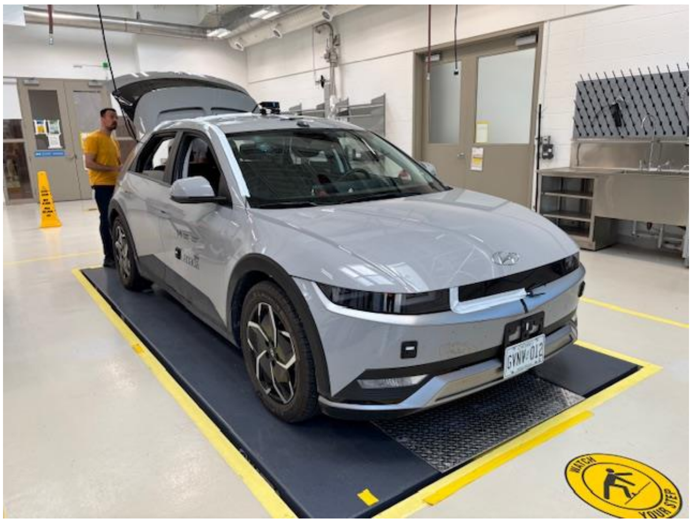

Figure 5: Instrumented test vehicle.

3.2 Test Conditions

On-road test data for this initial study were acquired between July 14 and 16, 2025, in the province of Ontario, Canada, on roadways between the cities of London and Sarnia. Most data were acquired on Highway 402, which is a four-lane divided highway oriented east-west, with combinations of open terrain and tree-lined segments, and a speed limit of 110 km/h. The target test conditions were constant-speed driving with various boundary conditions. Early-day testing was conducted, in lower-wind conditions, to target isolated constant-speed conditions with as little traffic as possible. Only data for which forward vehicles were estimated to be at a distance of at least 200 m, or more, were used for these “isolated” conditions, and larger distances for heavy trucks. Test runs of particular interest for this manuscript, and descriptions of the pertinent data segments, are:

- July 15, 2025, Run 01: Travelling westbound on Hwy 402, low traffic, relatively-low southerly winds (around 5 km/h or lower, from left to right).
- July 15, 2025, Run 02: Travelling eastbound on Hwy 402, low traffic, relatively-low southerly winds (around 5 km/h or lower, from right to left).

- July 15, 2025, Run 03: Travelling westbound on Hwy 402 in the wake of heavy trucks, relatively-low southerly winds (around 5 km/h or lower, from right to left).
- July 16, 2025, Run 01: Travelling westbound on Hwy 22 and Hwy 402 in the wake of light duty vehicles, moderate southerly winds (around 10 km/h or lower, from right to left).

3.3 Data Methods

Converting data from the BLE pressure sensors to useful pressure-coefficient-difference ($\Delta\bar{C}_P$) values required a number of data processing steps. A sample set of time-series data are provided in Figure 6 demonstrating measured data (speed, altitude, pressures) and processed data (pressure coefficients).

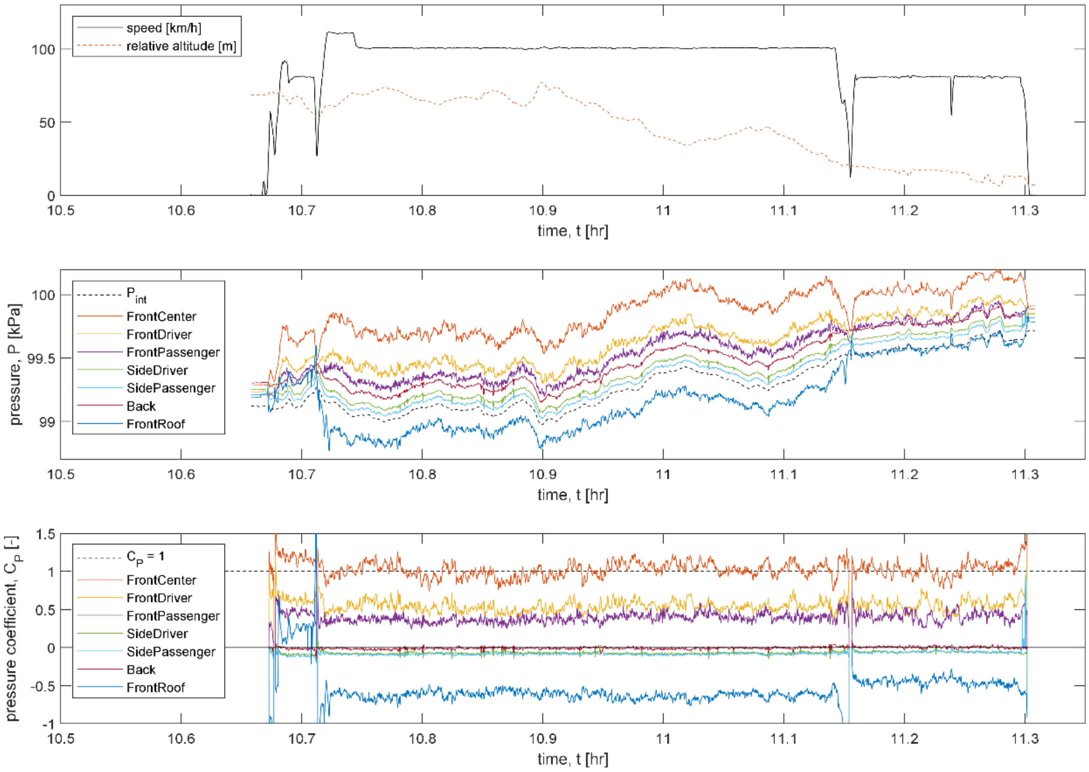

Figure 6: Subset of test data for Run 01 on July 15, 2025.

The top plot in Figure 6 shows the vehicle speed and its altitude profile for this test segment. The BLE pressure sensors measure absolute pressure (middle plot), and each has a small but quantifiable bias error, relative to the others, that drifts slightly over time. Furthermore, elevation changes and temporal changes due to the local climate generate variations in the pressure that can exceed the dynamic pressure of the apparent wind during testing. The hydrostatic pressure change associated with the 55 m altitude change (approx. 650 Pa) is equivalent to the dynamic pressure of a 120 km/h wind. To compensate for these various factors, to permit a reasonably-accurate calculation of the pressure coefficient for each sensor, a method to correct the measurements based on a reference pressure acquired internal to the cabin (P_{int} value in the middle plot, from the Xsens IMU sensor) was developed. The method is still under development, but its preliminary results provide a reasonable adjustment for each sensor. The C_P time-series data for each sensor are shown in the bottom plot of Figure 6. The Front Centre sensor, which resides near the stagnation point, provides a value near one, while the sides and base provide values near or slightly-below zero, providing reasonable validation of the approach. The Front Roof sensor shows the strongest sensitivity/uncertainty, with distinct offsets observed between the different-speed segments of the run. Although the metrics of interest for the transition-network methods are the pressure differences amongst the front, back, and side sensors ($\Delta\bar{C}_P$), and an accurate reference offset is not strictly necessary, these corrected C_P traces provide a means to interpret the aerodynamic behaviour of the vehicle based on conventional approaches, and permit spectral analysis of C_P signals for individual sensors.

4 On-Road Measurements

4.1 No-Traffic Conditions

To begin to understand the complex aerodynamic boundary conditions in the on-road data encountered by the test vehicle, the most basic case is analyzed. Isolated conditions for the on-road test can be assumed to have minimal cross/head wind, minimal interactions with other vehicles, and steady velocity. In Figure 7, on-road $\Delta\bar{C}_\mathrm{p}$ are plotted for steady-velocity data segments of low-wind test runs. The data are sorted by environmental conditions including estimated roadside tree density (colour) and vehicle direction (marker shape). Assuming that the low-wind conditions average to a no-wind result, 10 km/h wind limits on $\Delta\bar{C}_\mathrm{p}^{FB}$ are denoted about its mean and suggest that reasonably-low winds were encountered during these tests. The small range of $\Delta\bar{C}_\mathrm{p}^{FLR}$ and $\Delta\bar{C}_\mathrm{p}^{LR}$ values suggests low yaw angles, resulting from low winds, but the sensitivity of these parameters to yaw angle is unknown for this particular vehicle. Comparing these results to the DrivAer estimates in Figure 4, these results generally cluster within a range of $\Delta\bar{C}_\mathrm{p}$ values that indicate low winds. The general offset of the $\Delta\bar{C}_\mathrm{p}^{FLR}$ data towards positive values (about 0.1) is due to slight lateral asymmetries in the surface position and casing shape of the BLE sensors. Moderate linearity is observed between $\Delta\bar{C}_\mathrm{p}^{FLR}$ and $\Delta\bar{C}_\mathrm{p}^{LR}$, providing additional evidence that these state-space metrics may be suitable for transition-network analysis.

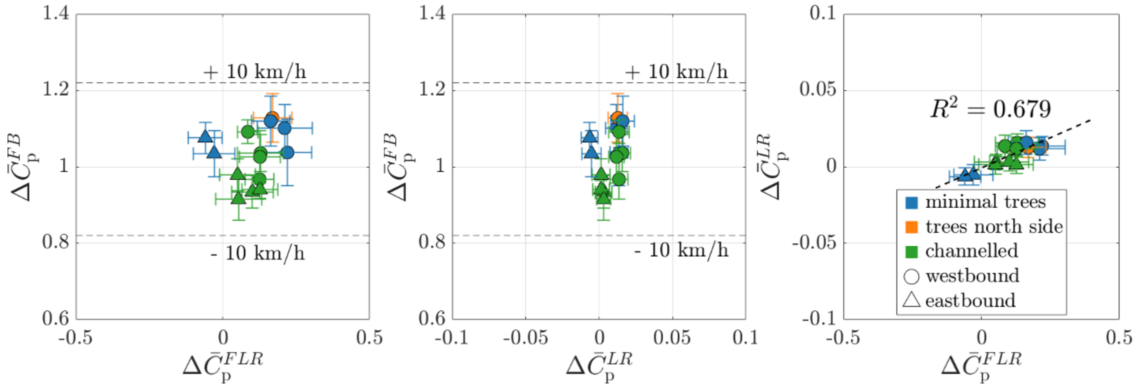

Figure 7: On-road $\Delta\bar{C}_\mathrm{p}$ plotted for isolated steady velocity data segments of Runs 01 and 02 July 15, 2025. Error bars represent one standard deviation.

4.2 Wake-Effects Conditions

To differentiate between close-proximity pressure-field influences and wake effects from leading vehicles such as an HDV or LDV, on-road $\Delta\bar{C}_\mathrm{p}$ parameters are plotted in Figure 8 for steady-velocity data segments for various following distances, all acquired on Hwy 402. On-road data are sorted by environmental conditions, with estimated roadside tree density encoded by marker colour, mean vehicle direction indicated by marker shape, and estimated following distance d represented by marker transparency. Error bars denote one standard deviation, reflecting the variability within each condition. Results show some clustering around the wind tunnel baseline $\Delta\bar{C}_\mathrm{p}$, as illustrated in Figure 4. Again, the dashed lines plotted in Figure 8 demonstrate expected $\Delta\bar{C}_\mathrm{p}^{FB}$ values under an assumption (±10 km/h wind speed) that this parameter behaves the same way for this test vehicle as it does for the wind-tunnel DrivAer model. The low $\Delta\bar{C}_\mathrm{p}^{FB}$ values suggest that wind-speed deficits in the LDV wakes reach about 10% of the driving speed, while in the HDV wakes they reach up to about 20%. The westbound LDV-wake data in regions with minimal trees show increased $\Delta\bar{C}_\mathrm{p}^{FLR}$ values with low $\Delta\bar{C}_\mathrm{p}^{FB}$ values, suggesting wake interactions with cross winds, but the $\Delta\bar{C}_\mathrm{p}^{LR}$ values do not show an increase as would be expected with cross winds based on its isolated-condition relationship to $\Delta\bar{C}_\mathrm{p}^{FLR}$ (right-side plot in Figure 6). Lateral shear in the wake, at small cross winds or small lateral offsets, may induce $\Delta\bar{C}_\mathrm{p}^{FLR}$ values indicative of cross winds when none are present. These results highlight the complexities of multi-condition interactions, and provide evidence that the three indicators selected ($\Delta\bar{C}_\mathrm{p}^{FB}$, $\Delta\bar{C}_\mathrm{p}^{FLR}$, and $\Delta\bar{C}_\mathrm{p}^{LR}$) may be insufficient to characterize adequately the aerodynamic state of the vehicle.

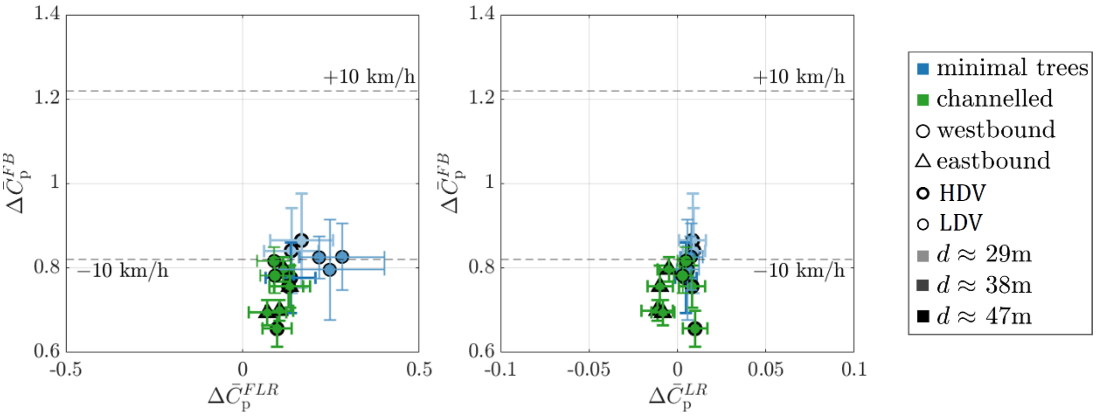

Figure 8: On-road $\Delta\bar{C}_\mathrm{p}$ parameters plotted for steady velocity data segments for following a LDV and HDVs. Test speeds between 100 km/h and 110 km/h.

As a secondary diagnostic of wake–proximity effects, power spectral densities (PSDs) of the pressure-differential metrics were computed. Welch’s method was used with a Hanning window and 75% overlap. This combination reduces noise but preserves resolution. The spectra are plotted in Figure 9 against reduced frequency, $f_r = fL/U$, where L corresponds to the width of vehicle being followed (estimates of 1.9 m used for LDVs and 2.6 m for HDVs) and U represents the steady vehicle speed. Significantly greater spectral energy is observed in the *FLR* metric (right plot) than for *FB* metric (left plot), due to the greater lateral coherence of wake turbulence across the front of the test vehicle than longitudinal coherence over its length. For the ‘following HDV’ cases, the spectra exhibit pronounced peaks at $\mathrm{St} = 0.076, 0.216, 0.260$ and 0.357. The energy clustering near $f_r = 0.2 \sim 0.24$ matches a previously derived band for HDV wakes [11].

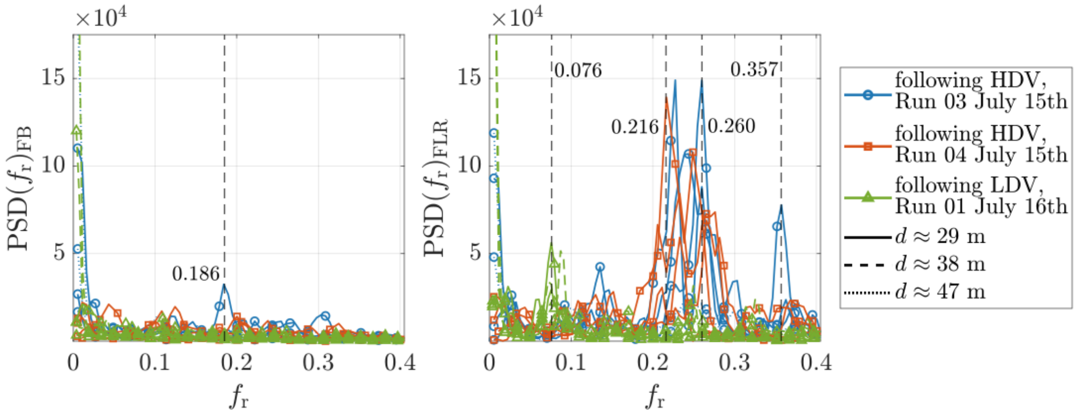

Figure 9: On-road pressure differential spectral analysis is plotted for steady velocity data segments for following an HDV and an LDV.

In contrast, for the ‘following LDV’ case (Run 01, July 16), peaks within the HDV band are absent or markedly weaker with only one pronounced peak at $\mathrm{St} = 0.186$, and the spectrum is more broadband. These differences are consistent with the smaller, less coherent wake of an LDV at the same streamwise spacing, possibly indicating stronger cross-flow fluctuations experienced by the test car due to wind.

4.3 Proximity-Effects Results

The proximity and relative position of other vehicles with respect to the test vehicle can impact greatly the measured $\Delta\bar{C}_\mathrm{p}$ parameters, as was shown for the DrivAer wind-tunnel data in Figure 4. A sample of proximity effects in on-road conditions are presented by looking at a segment of the July 15 tests (Run 01) where the test vehicle was in relatively-low wind conditions in a channeled-flow environment and was passed by an HDV. In Figure 10, $\Delta\bar{C}_\mathrm{p}$ time-series measurements are plotted to demonstrate the effect of the HDV position with respect to the test vehicle. The black dot with error bars represents the mean $\Delta\bar{C}_\mathrm{p}$ values and one standard deviation for this 45 s segment. The 0.1 offset in $\Delta\bar{C}_\mathrm{p}^{FLR}$ corresponds roughly with the sensor-position/shape bias noted in Section 4.1.

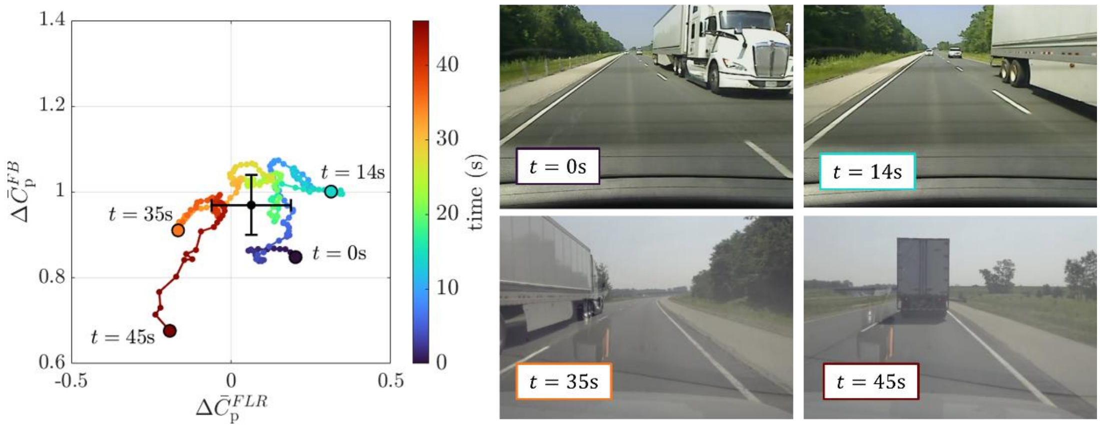

Figure 10: On-road $\Delta\bar{C}_\mathrm{p}$ parameters and respective mean values plotted for a steady velocity data segment where an HDV passed the test vehicle. Images show the progression of the passing maneuver and the effect the HDV position has on $\Delta\bar{C}_\mathrm{p}$ parameters over time.

With reference to published studies examining LDVs overtaking larger vehicles [12,13], and some of the author’s yet-to-be-published wind-tunnel work on LDV-HDV-proximity effects introduced in Section 2, the overtaking scenario in Figure 10 is explained. Each of the four highlighted positions correspond to an extreme in the $\Delta\bar{C}_\mathrm{p}$ parameters, identified by the timestamped images:

- *t* = 0 s, HDV behind test vehicle: The high-pressure field forward of the HDV increases the base pressure of the test vehicle, leading to $\Delta\bar{C}_{\mathrm{p}}^{FB}$ lower than 1, and displaces the airflow laterally causing an effective yaw angle for the vehicle, resulting in the positive $\Delta\bar{C}_{\mathrm{p}}^{FLR}$ values.
- *t* = 14 s, HDV approximately nose-to-nose with test vehicle: As the HDV begins to overtake the test vehicle, the combined blockage of the two-body system reduces the base pressure, increasing $\Delta\bar{C}_{\mathrm{p}}^{FB}$, and the flow-displacement effect of the HDV causes stronger local yaw angles, further increasing $\Delta\bar{C}_{\mathrm{p}}^{FLR}$.
- *t* = 35 s, test vehicle approximately nose-to-tail with the HDV: Localized blockage interactions between the vehicles generate reduced pressure over the front of the test vehicle, causing a decrease in $\Delta\bar{C}_{\mathrm{p}}^{FB}$, and concentrated more strongly on the left side, causing the change to negative $\Delta\bar{C}_{\mathrm{p}}^{FLR}$.
- *t* = 45 s: test vehicle behind HDV after it completes a lane change: Wake effects are introduced, lowering $\Delta\bar{C}_{\mathrm{p}}^{FB}$, and the lateral shear during the HDV-lane-change process is suspected to be the cause of the increasingly-negative $\Delta\bar{C}_{\mathrm{p}}^{FLR}$.

These individual $\Delta\bar{C}_P$ states may be interpreted differently if examined in isolation. For example, t = 0 s and 35 s states may be interpreted as wake-effect states with cross winds. However, the temporal transition between states provides additional context to the aerodynamic state of the vehicle, which is where transition-network concepts are expected to be beneficial for automated-vehicle control strategies.

5 Conclusions

This paper presented preliminary work towards a general concept for estimating the on-road aerodynamic state of a road vehicle, with anticipated uses for vehicle-automation technologies. On-road measurements were presented for three specific scenarios in relatively-low wind conditions, representing an isolated vehicle, following in the wakes of LDVs and HDVs, and being overtaken by an HDV. The measurements highlight that a combination of multiple metrics will be necessary to infer adequately the aerodynamic state of a vehicle. Complex conditions and varied positions of other vehicles in traffic highlight the need to track temporal changes in states, for which the use of transition networks will be applied to understand better, and to predict, aerodynamic states.

6 Reference list

[1] McTavish, S, Barber, H., Wall, A., “Field Measurements of the Airflow in the Urban Environment: An RPAS Use-Case in Montréal, Canada.”, Vertical Flight Society 80th Annual Form Proceedings, Montreal, Canada, May 2024, Paper 1133.

[2] Wang, Z., Bian, Y., Shladover, S.E., Wu, G., Li, S.E., Barth, M.J., 2019. “A survey on cooperative longitudinal motion control of multiple connected and automated vehicles.” IEEE Intelligent Transportation Systems Magazine,” doi:10.1109/MITS.2019.2953562.

[3] Bleckmann H, Zelick R. Lateral line system of fish. Integr Zool. 2009 Mar;4(1):13-25. doi: 10.1111/j.1749-4877.2008.00131.x. PMID: 21392273.

[4] Jessing, C., Wilhelmi, H., Wittmeier, F., Wagner, A. et al., “Investigation of Transient Aerodynamic Effects on Public Roads in Comparison to Individual Driving Situations on a Test Site,” SAE Technical Paper 2020-01-0670, 2020, doi:10.4271/2020-01-0670.

[5] Kaiser, F., Iacobello, G., and Rival, D.E., “Cluster-based Bayesian approach for noisy and sparse data: Application to flow-state estimation” Proc. R. Soc. A. , 48020230608 doi:10.1098/rspa.2023.0608.

[6] McAuliffe, B. and Barber, H., “Aerodynamic Drag of Road Vehicles in Close Lateral Proximity,” SAE Int. J. Advances & Curr. Prac. in Mobility 5(6):2004-2020, 2023, doi:10.4271/2023-01-0952.

[7] Le Good, G., Resnick, M., Boardman, P., Clough, B. et al., “Effects on the Aerodynamic Characteristics of Vehicles in Longitudinal Proximity Due to Changes in Style,” SAE Technical Paper 2018-37-0018, 2018, doi:10.4271/2018-37-0018.

[8] Chan, R., “On-road Aerodynamic State Estimation Using Sparse Pressure Sensors with Application to Truck Platooning,” M.A.Sc. Thesis, Queen’s University, Kingston, Ontario, Canada, 2023.

[9] McAuliffe, B. and Barber, H., “Simulating Traffic-wake Effects in a Wind Tunnel,” SAE Int. J. Advances & Curr. Prac. in Mobility 5(6):1969-1987, 2023, doi:10.4271/2023-01-0950.

[10] Ghorbanishohrat, F., McAuliffe, B., and O'Reilly, H., “Design and Evaluation of a Conceptual Zero-Emission Truck Model Considering Aerodynamic Efficiency,” SAE Technical Paper 2025-01-8784, 2025, doi:10.4271/2025-01-8784.

[11] Ficenec, K., McAuliffe, B., Lammert, M., and Holden, J., “Analysis of the Unsteady Wakes of Heavy Trucks in Platoon Formation and Their Potential Influence on Energy Savings,” SAE Technical Paper 2021-01-0953, 2021, doi:10.4271/2021-01-0953.

[12] Howell, J., Garry, K., and Holt, J., "The Aerodynamics of a Small Car Overtaking a Truck," SAE Int. J. Passeng. Cars - Mech. Syst. 7(2):2014, doi:10.4271/2014-01-0604.

[13] Shimizu, K., Nakashima, T., Hiraoka, T., Nakamura, Y. et al., “Investigation of Increase in Aerodynamic Drag Caused by a Passing Vehicle,” SAE Technical Paper 2018-01-0719, 2018, doi:10.4271/2018-01-0719.